Shaping the radiation pattern of second harmonic generation from AlGaAs dielectric nanoantennas

Luca Carletti[†], Andrea Locatelli[†], Dragomir Neshev[$], Costantino De Angelis[†].

[†]Department of Information Engineering, University of Brescia, via Branze 38, 25123 Brescia, Italy.

[$]Nonlinear Physics Centre, Research School of Physics and Engineering, The Australian National University, ACT 2601, Canberra, Australia

KEYWORDS (nanoantennas, nonlinear scattering, second harmonic generation, radiation pattern).

ABSTRACT. We study the manipulation of the radiation pattern of second harmonic generation from AlGaAs all-dielectric nanoantennas exhibiting electric and magnetic resonances. We show the importance of the interference of different higher-order multipoles in the nonlinear response of dielectric antennas for shaping of their second harmonic radiation pattern. In particular, we show how such multipolar interference can be engineered in AlGaAs nanodisks by manipulating the pump beam polarization, incidence angle and disk geometry. In this way we demonstrate the shaping of the radiation pattern in order to increase the second harmonic power by a factor of 8 when measured in experiment through a finite numerical aperture microscope objective.

A key property for the realization of compact photonic devices is the capability to manipulate light at the nanoscale. In past decades the advances in nanotechnology have allowed the realization of novel nanostructured materials such as plasmonic nanostructures, which have demonstrated the possibility to route and manipulate light in deep-subwavelength volumes[1–3]. However, while plasmonic nanostructures have met a huge success in many potential applications such as sensing, telecommunications, quantum-light sources, and photovoltaics[1–6], they suffer from ohmic losses at optical frequencies, which limit their efficiency[2,7]. Moreover, these losses generate Joule heating that could severely hamper the employment of plasmonics for some applications such as surface-enhanced Raman spectroscopy[8,9]. On the other hand, lossless dielectric materials can overcome this problem since their optical losses at visible and near-infrared wavelengths are negligible[7,10,11]. High-permittivity dielectric nanostructures in a low refractive index background can support strong Mie-type resonances[12] and can thus potentially be employed for nanophotonic applications, which are sensitive to the intrinsic losses and the generated heat, including biosensing, emission control and nonlinear frequency conversion[7,13,14]. Furthermore, dielectric nanoparticles can support both strong electric and magnetic resonances, which enable strong directional scattering by optical nanoantennas[15–21].

Importantly, all-dielectric nanostructures offer unique opportunities for the study of nonlinear effects. Due to the very low intrinsic losses, the dielectric nanostructures can sustain much higher optical powers and ultimately provide orders of magnitude higher frequency conversion efficiency[10,22] in comparison to their plasmonic counterparts. In addition, while in plasmonic nanostructures the optical nonlinear response is dominated by surface nonlinearities, enhanced by plasmon resonances at the fundamental and/or at the harmonic wavelengths[3,23–25], in high-permittivity dielectric nanostructures, the bulk nonlinearity may dominate the optical nonlinear

response[26]. Thus the overall interaction volume between the incident field and the nanostructure is highly increased, giving rise to better conversion efficiency. Most importantly, the efficiency of nonlinear conversion can be boosted even further by the excitation of multipolar resonant modes of both electric and magnetic nature[10,22,27,28].

These advantages have triggered a great interest into the studies of enhanced harmonic generation in resonant dielectric nanoparticles and very promising results have been recently achieved in simple all-dielectric structures[10,22,27,28] targeting applications in biosensing or nonlinear light sources. However, this important development is still in its infancy and there remain two important issues that have to be understood and carefully addressed. The first task is to achieve *high frequency conversion efficiencies*. While the efficiencies of third harmonic generation (THG) of 10^{-7} and 10^{-6} have been reported[10,29], which is 4-5 orders of magnitude higher than in plasmonic systems, these still remain low for most practical applications. For example, for biosensing applications efficiencies of the order of 10^{-2}-10^{-3} will be required in order to outperform the usual fluorescent markers. More recently, second harmonic generation (SHG) from subwavelength thickness AlGaAs nanodisks structures[22] has been predicted to reach efficiencies of 10^{-3} by exploiting the magnetic dipole resonance. Such efficiencies are comparable to the best achieved to date SHG efficiency in multiple quantum wells for intersubband transitions at mid-infrared wavelengths[30] and thus open a plethora of practical applications.

The second important issue is to be able to *shape the radiation pattern* of the harmonic generation, to direct it into desired directions, including achieving uni-directional harmonic generation from single nanostructures. This feature is of utmost importance as it measures the overall collection efficiency in the experiments, which is a practically meaningful value that is

related to the total detected signal. For example, in Ref. [22] a very high SHG efficiency was reported, however the second harmonic (SH) signal emitted was null in the both forward and backward directions, as schematically depicted on the left hand side of Fig. 1. This implies that if objectives with low numerical aperture (NA) are employed, most of the generated SH signal will be lost. For this reason, shaping the radiation pattern of SHG by enhancing the directivity or by reducing the angular spread of the generated signal, as schematically depicted on the right hand side of Fig. 1, will be fundamental for the employment of all-dielectric nanoantennas in applications requiring low power and low cost components such as chemical or biological sensing[7]. Despite the importance of this second point, the control and shaping of the radiation pattern from bulk nonlinearities in dielectric nanoparticles has gained little attention. While studies on the emission pattern of SHG scattering in centrosymmetric nanoparticles[31–34] and THG in amorphous dielectric particles[35] can be found in the literature, the shaping of the SHG radiation pattern in non-centrosymmetric dielectric nanoparticles, such as AlGaAs, remains unexplored.

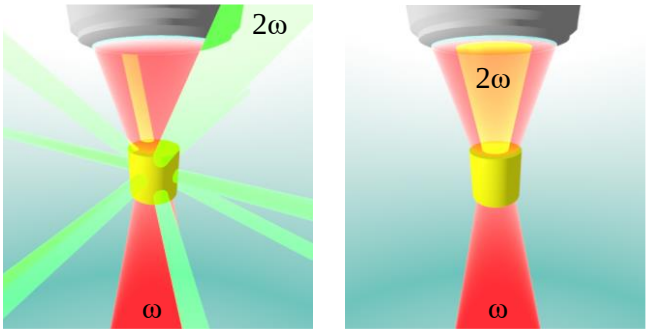

Figure 1. Conceptual representation of SH radiation pattern engineering. A red pump beam is focused by a microscope objective on the cylindrical nanoantenna. The SHG process generates green light that is emitted by the nanoantenna.

In this work we report on the shaping of the radiation pattern of SHG in AlGaAs nanostructures. The multipolar nature of the optical nonlinear response in all-dielectric nanostructures can be harnessed for improving the directivity of the SH signal emitted by nanoantennas. In the first part we show how to control the SH emission pattern by changing the pump polarization state and how to achieve directional SH emission by exploiting multipolar electric and magnetic interference. In the second part we show that by using a tilted pump beam one can obtain radiation patterns that have a maximum in the normal forward and backward directions. Our results open new opportunities for highly efficient nonlinear light sources with controlled emission characteristics.

RESULTS AND DISCUSSION

Numerical simulations

To demonstrate the control of the radiation pattern of SH field generated by $Al_{0.18}Ga_{0.82}As$ nanoantennas we use frequency-domain simulations implemented using the finite-element-method in COMSOL[22]. In our simulations we consider a single AlGaAs antenna in air (refractive index n=1) and use perfectly matched layers to implement open boundary conditions. The real and imaginary part of the AlGaAs susceptibility are deduced from Refs. [36,37]. The pump is assumed to be a plane wave, s-polarized along one of the crystalline axes, which in our simulations are aligned with Cartesian coordinate system axes. The second-order nonlinear susceptibility tensor of AlGaAs has only off-diagonal elements of the type $\chi_{ijk}^{(2)}$ with $i \neq j \neq k$. Thus the *i-th* component of the nonlinear polarization at the SH frequency 2ω is given by[22]

$$P_i^{(2\omega)} = \varepsilon_0 \chi_{ijk}^{(2)} E_j^{(\omega)} E_k^{(\omega)}, \quad (1)$$

where ε_0 is the vacuum dielectric constant and $E_j^{(\omega)}$ is the *j-th* component of the electric field at the pump frequency ω. The value of $\chi_{ijk}^{(2)}$ used in the simulations is 100 pm/V and it is assumed to be constant over all the range of pump wavelengths that is considered in this work[38,39].This cross-term nonlinear susceptibility tensor displays an unique characteristic of the AlGaAs material, as the nonlinear polarization does not follow the symmetry of the incident field and distinguishes our problem from the works on THG[35]. The nonlinear polarization in Eq. (1) is used to define the nonlinear source currents and calculate the SHG in the AlGaAs cylinders.

Normal incidence excitation

To help the reader it is worth reproducing some of the results from Ref. [22]. Figure 2(a) shows the SHG efficiency and the linear scattering efficiency as a function of pump wavelength for an AlGaAs cylinder with a radius of 225 nm and a height of 400 nm. The maximum SHG efficiency is achieved for a pump wavelength of about 1685 nm that is close to the magnetic resonance, which is at a wavelength of about 1650 nm. In the range of the SH wavelengths, however a multitude of modes exist, which can be excited or not depending on the symmetry of the nonlinear polarization induced by the pump beam. The radiation pattern of the SH signal is shown in Figs. 2(b) and 2(c) and is characterized by multiple SH lobes and no SH light that is emitted in the normal forward and backward directions. Figure 2(d) shows the nonlinear displacement current density inside the AlGaAs cylinder. The nonlinear current distribution is symmetric with respect to the *xz* and *xy* planes and gives rise to a nonlinear source that resembles an electric quadrupole. This displacement current distribution leads to excitation of modes that are in opposition of phase and thus have a zero in the normal forward and backward directions. The electric field at the SH wavelength is shown in Fig. 2(e). From the tangential components of

the electric field on the cylinder walls one can deduce the far-field pattern. In particular we can recognize the electric quadrupolar field lines on the lateral walls as well as on top and bottom walls.

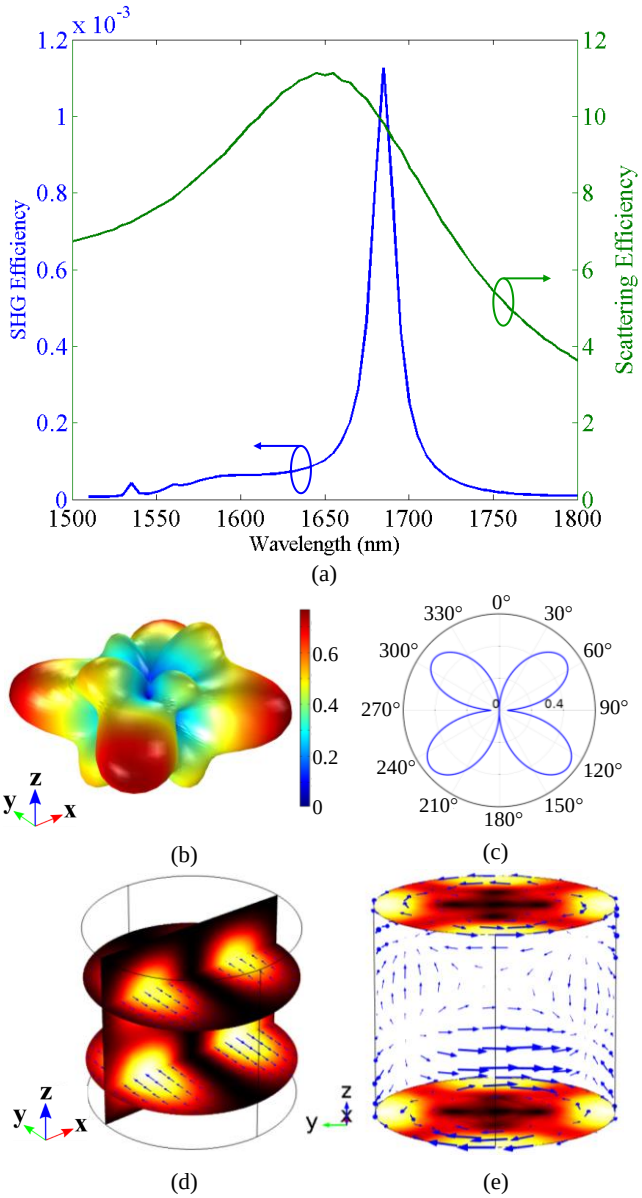

Figure 2. (a) SHG efficiency and linear scattering efficiency as a function of wavelength. (b) Radiation diagram of the SH electric field. Color scale represents absolute value of the electric field. (c) Radiation diagram in the *xz* plane plotted in polar coordinates (θ=0° is +*z*-axis direction and θ=90° is +*x*-axis direction). The radial distance represents the absolute value of the

electric field. (d) Nonlinear displacement current in the cylinder induced by the pump field. (e) Electric field distribution at the SH wavelength. The blue arrows represent the electric field tangent to the cylinder walls. The results are obtained using a cylinder, oriented with its axis in the z-axis direction, with h=400 nm, r=225 nm and for a normally incident plane wave pump polarized along the x-axis and with an intensity of 1 GW/cm^2. Results from (b) to (e) are obtained for a pump wavelength of 1685 nm.

The radiation pattern of the SH field depends on the mode that is excited by the nonlinear polarization induced by the fundamental mode. Thus, if the electric field distribution inside the cylinder at the fundamental frequency is changed, a different mode at the SH frequency may be excited. This effect could be obtained either by changing the incident pump beam (polarization state, wavevector or spatial structure) or by changing the shape and geometry of the dielectric antenna, hence altering its electromagnetic modes at the pump and SH wavelengths. Below we show how the SH radiation pattern is affected when changing each of these parameters.

Radiation pattern manipulation by changing the pump polarization state

The observation of SHG as a function of the polarization state of the pump beam was demonstrated to be a powerful tool for imaging of nano-objects[40] and semiconductor nanowires[41]. Inspired by these results we investigate how the beam polarization state may alter the emission diagram of the SH signal from AlGaAs nanoantennas. Figure 3(a) shows the SHG efficiency as a function of the wavelength and the pump polarization state. For a pump beam, which is linearly polarized along one of the crystalline axes, orthogonal to the cylinder axis, there is only one peak of SHG efficiency at a wavelength of 1685 nm[22] (see also Fig. 2(a)). In comparison, for a pump beam linearly polarized along the bisector of the crystalline axes, two

SHG peaks can be observed in the spectrum. The strongest peak is the same as in the first case. The second, weaker, peak that is obtained at a pump wavelength of about 1580 nm corresponds to a different SH mode that could not be excited with the pump linearly polarized along one of the crystalline axes. Figure 3(b) shows the radiation pattern of this mode, which is radically different from the SH radiation pattern that is shown in Fig. 2(a). Moreover, as it can be seen from Fig. 3(a), by using a pump with circularly polarized electric field only the SH peak at 790 nm can be observed while a different SH radiation pattern is obtained when pumping at a wavelength of 1685 nm (compare Fig. 3(c) with Figs. 3(b) and 2(b)).

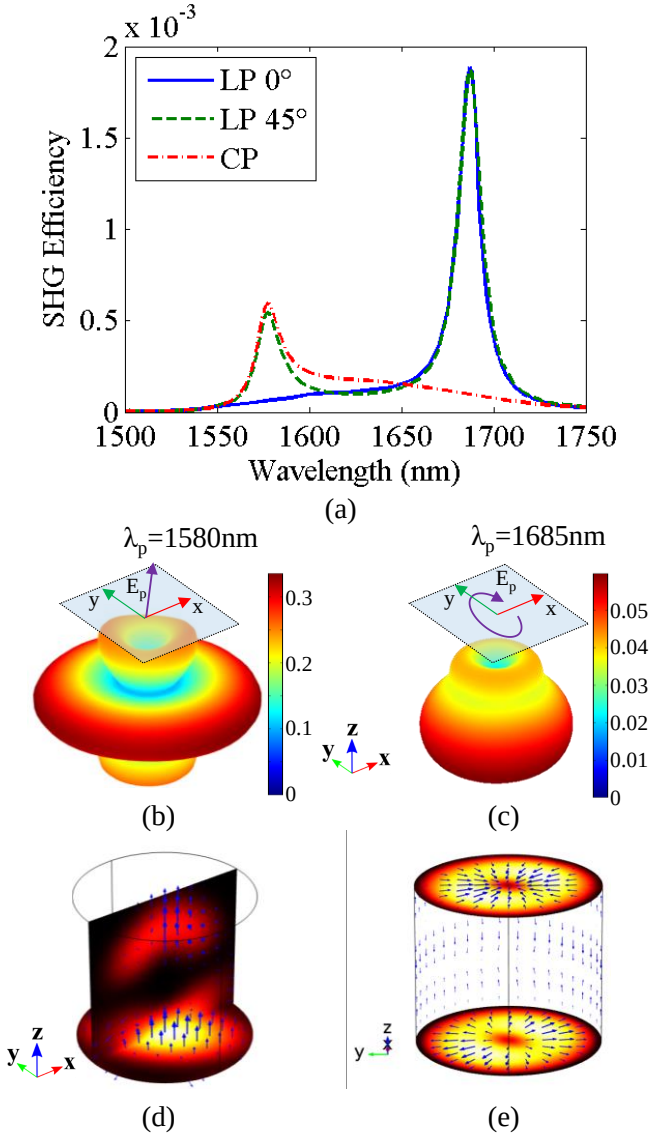

Figure 3. (a) SHG efficiency as a function of wavelength and polarization state for a cylinder with h=400 nm and r=225 nm. Pump polarization states are: LP 0° for linear polarization along x-axis; LP 45° for linear polarization along xy-plane bisector; CP for circularly polarized light. (b) Radiation diagram of the SH electric field for LP 45° pump at a wavelength of λ_p=1580 nm. (c) Radiation diagram of the SH electric field for pump with circular polarization at a wavelength of λ_p=1685 nm. The incident electric field polarization is depicted by the E_p arrow. (d) Nonlinear displacement current generated in the cylinder by the pump field for LP 45° pump at a wavelength of 1580 nm. The color scale depicts the absolute value of the nonlinear current. (e) Electric field at the SH wavelength using LP 45° pump at a wavelength of 1580 nm. The blue arrows represent the electric field tangent to the cylinder walls.

The excitation of different modes when changing the pump polarization state is a consequence of a variation of the nonlinear displacement currents that are induced by the fundamental mode via the nonlinear susceptibility. Figure 3(d) shows the nonlinear displacement currents induced by a pump at a wavelength of 1580 nm with linearly polarized electric field aligned on the bisector between the x and y crystalline axes. As it can be seen, the main component of the nonlinear displacement current is along the cylinder axis. In comparison, the nonlinear displacement current generated with a pump beam, which is linearly polarized along the x axis, has mainly a y axis component as shown for instance by the blue arrows in Fig. 2(d). This difference in the nonlinear displacement current distribution is due to the form of the $\chi^{(2)}$ tensor of AlGaAs that results in a nonlinear polarization of the form given by Eq. (1). As seen in Fig. 3(a), the SH intensity obtained for a pump wavelength of 1685 nm is the same for both LP 0° and LP 45° polarization states. This is due to several reasons: First, the electric field of the SH mode excited at 842.5 nm has a predominant radial component, thus only nonlinear currents in

the *xy* planes will be able to efficiently excite this mode. Second, the antenna has a cylindrical symmetry, which implies that there is not any linear birefringence effect. Thus the LP 45° pump can be seen as the sum of two in-phase pumps with polarization state LP 0° and LP 90°, which is equivalent to the situation of having just one pump with LP 0° polarization and hence will result to the same SHG efficiency. On the other hand, the SH mode at 842.5 nm is not excited by the CP pump because this case corresponds to two pumps with polarization state LP 0° and LP 90° of $\pi/2$ out of phase. This results in an azimuthal distribution of the nonlinear displacement currents in the *xy* planes that does not couple efficiently to the SH mode at 842.5 nm. In general, more complex pump polarization states might be used to control the nonlinear displacement current distribution inside the antenna and thus to engineer the radiation pattern of the SH field.

Figure 3(e) shows the tangential electric field on the cylinder walls. The resonant modes in the cylinder might be interpreted as guided modes of the cylindrical rod that are back reflected at the cylinder basis. Thus a resonance appears in the spectrum when the optical length of the rod is about a multiple of $\lambda_g/2$ where $\lambda_g=\lambda/n_{eff}$ and n_{eff} is the effective index of the mode. For instance we can recognize a similarity between the electric field on the top surface of the cylinder in Fig. 3(e) and the electric field of a TM_{01} mode in fibers. Indeed, at the SH wavelength (i.e. λ=790 nm) the optical length of the cylinder is approximately $1.5\times\lambda_g$ (n_{eff}=2.84). However this classification might be difficult when the excited mode is the superposition of several modes, as in the case of the SH excited with a pump wavelength of 1685 nm, shown in Fig. 2(e). Nevertheless, this mode distribution can still be connected to the HE_{21} mode and the optical length of the cylinder in this case is about $1.3\times\lambda_g$ (n_{eff}=2.74).

Radiation pattern manipulation by changing the antenna geometry

Even though we showed that it is possible to excite different modes by changing the polarization state of the pump, the radiation patterns shown in Figs. 2(b) and 3(b) do not exhibit any forward or backward directivity. Since in typical microscopy applications the signal collection is usually performed on one side of the device, a directive emission diagram might be desirable in order to increase the collection efficiency of the SH signal. One method that has been proposed for achieving this feature in the optical response of an antenna is to exploit the relative phase difference of the electric field emitted by an electric dipole and a magnetic dipole resonance[15,16,21]. This phase difference gives rise to an interference of several radiating multipoles, which can be used to achieve directional SH emission. In particular, the interference effect is enhanced when the so-called Kerker condition is satisfied[42]. This requires that the light is radiated as a superposition of equal strength of both electric and magnetic dipoles. The Kerker principle has also been extended to interference of higher order multipoles, finding that whenever multipoles with the same amplitude and opposite symmetry are present, the emission diagram becomes highly directive[16,21]. Nevertheless, some degree of directionality can be practically achieved even when the optical response is composed by a few multipoles of comparable strength[21]. Here we exploit this phenomenon to illustrate how the generalized Kerker conditions can be applied to achieve a directional emission of the SH signal that is generated in AlGaAs nanoantennas. Figure 4(a) shows the extinction efficiency of a cylindrical nanoantenna with a radius r=146 nm and height h=400 nm. As it can be seen, for this cylinder dimensions, the magnetic dipole resonance is around a wavelength of 1235 nm. Furthermore, at half of this wavelength, corresponding to the range of SH emission, the electric and magnetic dipole and quadrupole (i.e. a_1, b_1, a_2, and b_2 Mie-type coefficients) have similar amplitudes. This condition not only ensures an enhancement of the SHG due to a pump wavelength that is tuned on the MD

resonance of the nanoantenna, but it also results in a directive forward emission diagram of the electric field, as shown by the radiation pattern in the inset of Fig. 4(a). As seen from Figs. 4(b) and 4(c) this allows the generation of a directive SH emission when pumping at a wavelength of 1235 nm.

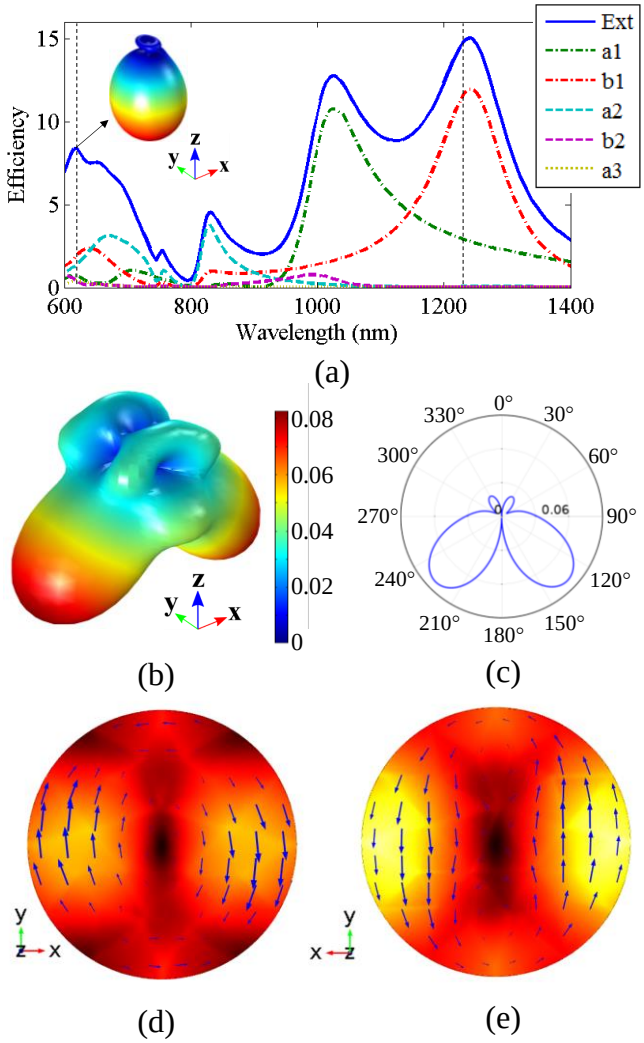

Figure 4. (a) Extinction efficiency as a function of wavelength for a cylinder with h=400 nm and r=146 nm. The decomposition of the scattering efficiency in electric and magnetic multipoles is shown in the right-hand side of the figure. The coefficients a_1 and b_1 represent the amplitude of the electric and magnetic dipoles (dashed-dotted lines), a_2 and b_2 represent the amplitudes of the electric and magnetic quadrupoles (dashed lines), and a_3 represents the amplitude of the electric

octupole (dotted line). (b) Radiation diagram of the SH field for a pump at 1235 nm. The color scale represents the absolute value of the electric field. (d, e) Absolute value of the electric field on the top and bottom surface of the cylinder. The arrows show the tangential electric field. The results are obtained for a normally incident plane wave pump at a wavelength of 1235 nm with an electric field polarized along the *x* axis.

In order to gain deeper insight on the physical mechanisms that are responsible for this nonlinear optical response, in Figs. 4(d) and 4(e) we plot the electric field on the top and bottom surfaces of the cylinder, respectively. On the top surface (see Fig. 4(d)) we can recognize a dominant electric quadrupolar field distribution, where the electric field components along the *y* axis are larger than the components of the electric field that are along the *x* axis. On the bottom surface (see Fig. 4(e)) the electric field distribution is dominated by a magnetic dipole. The field components that are symmetric with respect to the *y* axis are dominating, like on the top surface. However the field symmetric with respect to the *x* axis has opposite phase with respect to the top surface. This is due to the interference between magnetic and electric multipoles, which is constructive in the forward direction while is destructive in the backward direction. Furthermore, the in-plane radiation is almost suppressed compared to the case shown in Fig. 2(b).

Although this configuration addresses the problem of directive SHG emission, two other issues arise: first, the total SHG efficiency is reduced by a factor of 100 as compared to Ref [22], and second, in the normal forward and backward direction the SH signal remains zero. The decrease of the SHG efficiency is due to a poor overlap between the fundamental and the SH mode. Instead, the second problem is due to the symmetry of the extrinsic geometry - antenna

plus pump excitation; as well as due to the form of the susceptibility tensor of AlGaAs. Therefore in the next section we analyze what happens when this extrinsic symmetry is broken.

Radiation pattern manipulation for tilted incidence pump

A possible solution to break the symmetry that forced the SH radiation to be zero in forward and backward directions is to use a tilted pump beam. In this case the extrinsic or "experimental" symmetry is broken. Figure 5 shows the evolution of the radiation pattern of the SH signal generated with an s-polarized pump at a wavelength of 1570 nm, for a varying angle of incidence θ on a cylinder with r=225 nm and h=400 nm.

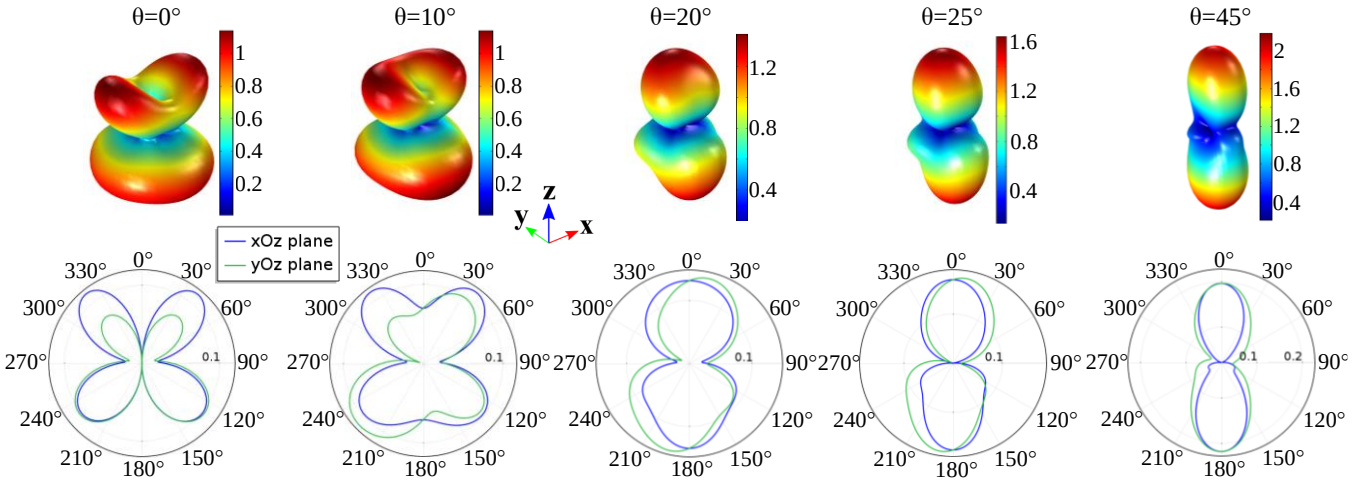

Figure 5. Top line: radiation patterns of the SH signal as a function of the angle of incidence θ. The color scale represents the absolute value of the electric field. Bottom line: radiation patterns in the xz plane (blue line) and yz plane (green line). The results are obtained using a cylinder with h=400 nm, r=225 nm and for a pump at a wavelength of 1570 nm. The electric field is polarized along the x-axis.

The case with pump at normal incidence (θ=0°) shows multipolar behavior of the SH radiation with the expected zero in the normal forward and normal backward direction. As the angle of incidence increases, the SH field emitted in the normal directions increases, reaching a maximum at θ=45°, while the lobes in the other directions are progressively suppressed. This behavior may be understood by observing the scattering efficiency of the cylinder at the SH wavelengths and the electric field generated inside the cylinder. Figure 6(a) shows the linear scattering efficiency of the cylinder for wavelengths in the range of the SH emission. From the multipole expansion of the scattered field that is also reported in Fig. 6(a), we can observe that the peak of scattering efficiency at a wavelength of 785 nm is mainly due to an electric dipole resonance. The electric field radiation diagram at this wavelength (shown in the inset of Fig. 6(a)) is constituted by two main lobes; one in the forward and one in the backward direction. The *x*-component of the electric field at a wavelength of 785 nm inside the cylinder as derived from the linear simulations is shown in Fig. 6(b). For comparison, Fig. 6(c) shows the *x*-axis component of the electric field generated in the SHG process for a pump with angle of incidence θ=45°. The two field distributions remarkably resemble each other, indicating that the nonlinear currents generated by the tilted pump couple to the mode observed in the extinction spectrum of Fig. 6(a) that was characterized in the far-field by single forward and backward lobes.

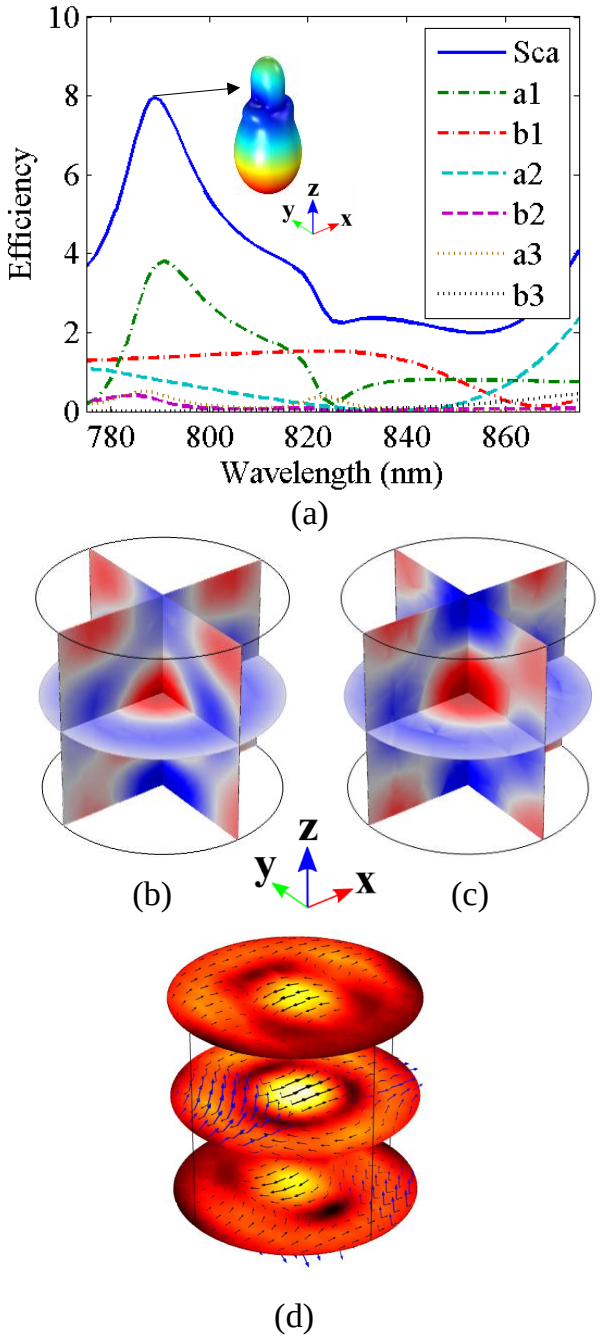

Figure 6. (a) Scattering efficiency as a function of wavelength for a cylinder with h=400 nm and r=225 nm excited by a plane wave at normal incidence. The electric, a, and magnetic, b, dipole (dashed-dotted lines), quadrupole (dashed lines), and octupole (dotted line) decomposition of the scattering efficiency is also shown in the figure. The inset shows the far-field diagram at λ=785 nm. (b) Electric field (E_x) in the cylinder at λ=785 nm. (c) Electric field ($E_x^{(2\omega)}$) at the SH

generated in the cylinder using a pump at λ=1570 nm and with an angle of incidence of θ=45°. (d) Absolute value of the electric field generated at the SH with a pump at λ=1570 nm. The black arrows represent electric field vectors and blue arrows represent the nonlinear displacement currents.

Figure 6(d) shows the electric field at the SH frequency that is generated using a pump at λ=1570 nm. In particular, by observing the electric field on the top and bottom surfaces, we can see that the emitted SH radiation is mainly of electric dipole type with an electric field polarized along the *x*-axis, in agreement with the far-field shown for θ=45° in Fig. 5.

In order to assess the advantage of the SHG using tilted pump incidence versus normal incidence pump, we evaluate the SH collection efficiency in a realistic experimental setting, e.g. the power that would be collected from the nanoantenna in transmission by using a collection microscope objective with a NA of 0.25. This value of the NA is chosen since it can be achieved with typical low-cost optical components. Figure 7(a) shows the measurable SH power as a function of pump wavelength and cylinder radius under these experimental conditions. In these calculations the cylinder height and the angle of incidence of the s-polarized pump are kept constant at 400 nm and 45°, respectively. The pump intensity is 1 GW/cm^2. As it can be seen in Fig. 7(a) the peak of SH transmitted power reaches the value of 38 μW for a cylinder with r=195 nm and pump wavelength of 1470 nm. For comparison, the SH transmitted power using a pump at normal incidence on a cylinder with r=225 nm (as in Ref [22]) is only about 5 μW, a factor of 8 times smaller. The SH peak observed for a cylinder with r=195 nm and a pump wavelength of 1470 nm in Fig. 7(a) is due to the electric dipole mode radiation, as seen in Fig. 5 for θ=45°. The SHG efficiency calculated for a tilted incident pump is shown in Fig. 7(b). We can observe

that the SHG efficiency values are similar to the ones in Ref. [22]. Furthermore, it should be noted that the highest SH power emitted in forward direction is not achieved with the configuration that results in highest SHG efficiency (compare Figs. 7(a) and (b)). This is because the SHG efficiency is calculated by integrating all the SH signal over the entire solid angle, while the forward radiated SH power is only the fraction of SH signal that is emitted within the NA of the objective. This numerical experiment shows that the tilted pump configuration can be more advantageous than the normal incidence configuration.

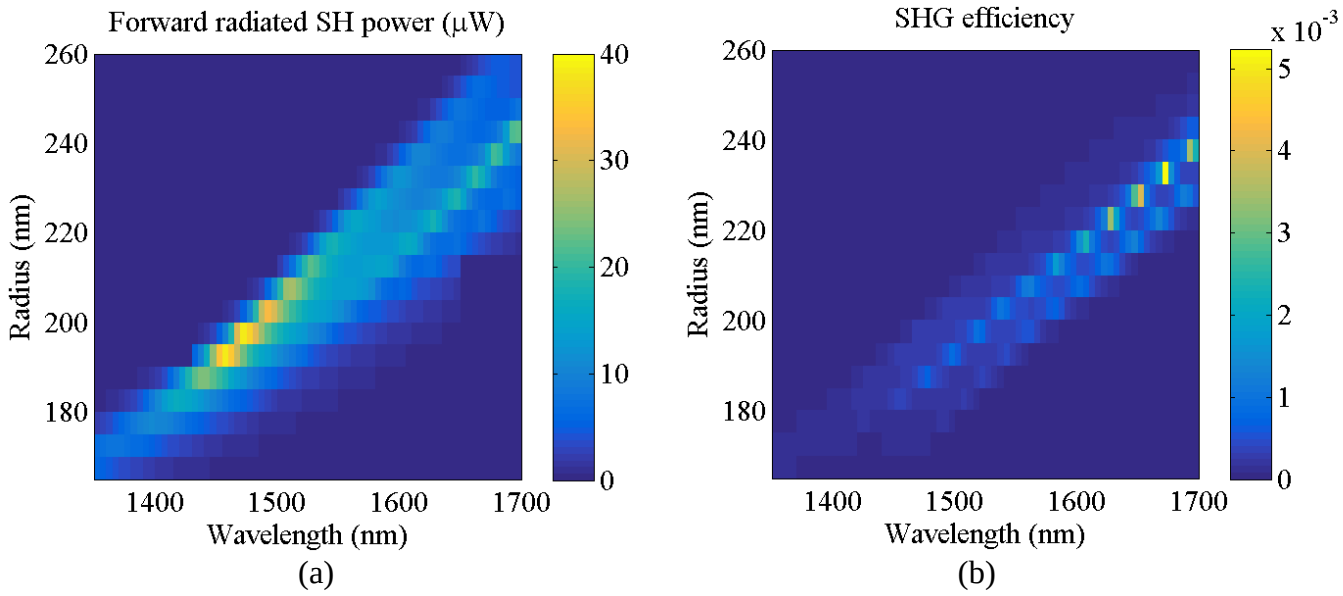

Figure 7. (a) Forward radiated SH power as a function of pump wavelength and cylinder radius. (b) SHG efficiency as a function of pump wavelength and cylinder radius. The calculations are performed using an s-polarized pump that is incident on the cylinder at an angle of 45° with respect to the cylinder axis. NA of the objective is fixed to 0.25.

CONCLUSIONS

In summary, we have demonstrated numerically the possibility to shape the radiation pattern of the SH field generated by an AlGaAs cylindrical nanoantenna. We have found that by modifying

the polarization state of the incident light we can excite different modes at the SH frequency, therefore altering the spectral response of the SH conversion efficiency as well as the directionality of the SH emission. Furthermore, we have shown that by exploiting the interference effects of magnetic and electric multipoles sustained by the nanoantenna at the SH frequency, we can obtain uni-directional emission of SH. However, the structural symmetry and properties of the nonlinear susceptibility of AlGaAs pose strict restrictions on the emission pattern and no SH emission could be generated in the normal forward or backward directions.

Finally, we have demonstrated that by breaking the extrinsic symmetry of the structure plus the incident beam, e.g. by using a pump beam at tilted incidence, this issue can be overcome. This configuration not only allows one to obtain a SH signal in the normal directions, but also to increase the detectable SH power. To illustrate this, we have calculated the power collected in transmission by a microscope objective with NA= 0.25. We have seen that the detected SH power can be 8 times larger than by using a pump at normal incidence. This effect can be advantageous under several aspects. In particular it allows reducing the pump power that is required for obtaining a particular level of SH power.

This may benefit several applications such as nonlinear spectroscopy of chemical and biological species where excessive level of pump powers may alter or even induce damage to the analyzed sample. We expect that further opportunities for the control of the radiation pattern can be achieved by implementing structured light pump beams with tailored polarization properties.

AUTHOR INFORMATION

Corresponding Author

*E-mail: luca.carletti@unibs.it

Author Contributions

The manuscript was written through contributions of all authors. All authors have given approval to the final version of the manuscript.

Funding Sources

The paper and the participation of all the authors has been made in the framework of the Erasmus Mundus NANOPHI project, contract number 2013 5659/002-001. L. Carletti, C. De Angelis and A. Locatelli acknowledge financial support from U.S. Army ("Engineering second order nonlinear effects in optical antennas") and CARIPLO ("SHAPES - Second-HArmonic Plasmon-Enhanced Sensing"). D. N. Neshev acknowledges the support of the Australian Research Council and of the Visiting Program of the University of Brescia

ACKNOWLEDGMENT

We thank M. Finazzi, Y. Kivshar, and G. Leo for the useful discussions.

ABBREVIATIONS

SHG, second harmonic generation; SH, second harmonic; NA, numerical aperture; THG, third harmonic generation

REFERENCES

[1] Zhang, J. Z.; Noguez, C. Plasmonic optical properties and applications of metal nanostructures. *Plasmonics* **2008**, 3, 127–150.

[2] Schuller, J. A.; Barnard, E. S.; Cai, W.; Jun, Y. C.; White, J. S.; Brongersma, M. L. Plasmonics for extreme light concentration and manipulation. *Nat. Materials* **2010**, 9, 193–204.

[3] Kauranen, M.; Zayats, A. V. Nonlinear Plasmonics. *Nat. Photonics* **2012**, 6, 737–748.

[4] Atwater, H. A.; Polman, A. Plasmonics for improved photovoltaic devices. *Nat. Materials* **2010**, 9, 205–213.

[5] Anker, J. N.; Hall, W. P.; Lyandres, O.; Shah, N. C.; Zhao, J.; Van Duyne, R. P. Biosensing with plasmonic nanosensors. *Nat. Materials* **2008**, *7*, 442–453.

[6] Giannini, V.; Fernández-Domínguez, A. I.; Heck, S. C.; Maier, S. A. Plasmonic nanoantennas: Fundamentals and their use in controlling the radiative properties of nanoemitters. *Chem. Rev.* **2011**, 111, 3888–3912.

[7] Albella, P.; Alcaraz de la Osa, R.; Moreno, F.; Maier, S. A. Electric and Magnetic Field Enhancement with Ultralow Heat Radiation Dielectric Nanoantennas: Considerations for Surface-Enhanced Spectroscopies. *ACS Photonics* **2014**, 1, 524–529.

[8] Huang, Y. F.; Zhu, H. P.; Liu, G. K.; Wu, D. Y.; Ren, B.; Tian, Z. Q. When the signal is not from the original molecule to be detected: Chemical transformation of para-Aminothiophenol on ag during the SERS measurement. *J. Am. Chem. Soc.* **2010**, 132, 9244–9246.

[9] King, M. D.; Khadka, S.; Craig, G. A.; Mason, M. D. Effect of Local Heating on the SERS Efficiency of Optically Trapped Prismatic Nanoparticles. *J. Phys. Chem. C* **2008**, 112, 11751–11757.

[10] Shcherbakov, M. R.; Neshev, D. N.; Hopkins, B.; Shorokhov, A. S.; Staude, I.; Melik-Gaykazyan, E. V.; Decker, M.; Ezhov, A. A.; Miroshnichenko, A. E.; Brener, I.; Fedyanin

A. A.; Kivshar Y. S. Enhanced Third-Harmonic Generation in Silicon Nanoparticles Driven by Magnetic Response. *Nano Lett.* **2014**, 14, 6488–6492.

[11] Ginn, J. C.; Brener, I.; Peters, D. W.; Wendt, J. R.; Stevens, J. O.; Hines, P. F.; Basilio, L. I.; Warne, L. K.; Ihlefeld, J. F.; Clem, P. G.; Sinclair, M. B. Realizing optical magnetism from dielectric metamaterials. *Phys. Rev. Lett.* **2012**, 108, 097402.

[12] Bohren, C. F.; Huffman, D. R., *Absorption and Scattering of Light by Small Particles*, Wiley-VCH Verlag GmbH, 1998.

[13] Caldarola, M.; Albella, P.; Cortés, E.; Rahmani, M.; Roschuk, T.; Grinblat, G.; Oulton, R. F.; Bragas, A. V.; Maier, S. A. Non-plasmonic nanoantennas for surface enhanced spectroscopies with ultra-low heat conversion. *Nat. Communications* **2015**, 6, 7915.

[14] Bakker, R. M.; Permyakov, D.; Yu, Y. F.; Markovich, D.; Paniagua-Domínguez, R.; Gonzaga, L.; Samusev, A.; Kivshar, Y. S.; Luk`yanchuk, B.; Kuznetsov, A. I.; Magnetic and Electric Hotspots with Silicon Nanodimers. *Nano Lett.* **2015**, 15, 2137–2142.

[15] Staude, I.; Miroshnichenko, A. E.; Decker, M.; Fofang, N. T.; Liu, S.; Gonzales, E.; Dominguez, J.; Luk, T. S.; Neshev, D. N.; Brener, I.; Kivshar Y. Tailoring directional scattering through magnetic and electric resonances in subwavelength silicon nanodisks. *ACS Nano* **2013**, 7, 7824–7832.

[16] Alaee, R.; Filter, R.; Lehr, D.; Lederer, F.; Rockstuhl, C. A generalized Kerker condition for highly directive nanoantennas. *Opt. Lett.* **2015**, 40, 2645-2648.

[17] Lee, K. G.; Chen, X. W.; Eghlidi, H.; Kukura, P.; Lettow, R.; Renn, A.; Sandoghdar, V.; Götzinger, S. A planar dielectric antenna for directional single-photon emission and near-unity collection efficiency. *Nat. Photonics* **2011**, 5, 166–169.

[18] Yan, J.; Liu, P.; Lin, Z.; Wang, H.; Chen, H.; Wang, C.; Yang, G. Directional Fano

Resonance in a Silicon Nanosphere Dimer. *ACS Nano* **2015**, 9, 2968–2980.

[19] Fu, Y. H.; Kuznetsov, A. I.; Miroshnichenko, A. E.; Yu, Y. F.; Luk'yanchuk, B. Directional visible light scattering by silicon nanoparticles. *Nat. Communications* **2013**, 4, 1527.

[20] Rolly, B.; Stout, B.; Bonod, N. Boosting the directivity of optical antennas with magnetic and electric dipolar resonant particles. *Opt. Express* **2012**, 20, 20376-20386.

[21] Liu, W.; Zhang, J.; Lei, B.; Ma, H.; Xie, W.; Hu, H. Ultra-directional forward scattering by individual core-shell nanoparticles. Opt. Express **2014**, 22, 16178.

[22] Carletti, L.; Locatelli, A.; Stepanenko, O.; Leo, G.; De Angelis, C. Enhanced second-harmonic generation from magnetic resonance in AlGaAs nanoantennas. *Opt. Express* **2015**, 23, 26544- 26550.

[23] Butet, J.; Brevet, P. F.; Martin, O. J. F. Optical Second Harmonic Generation in Plasmonic Nanostructures: From Fundamental Principles to Advanced Applications. *ACS Nano* **2015**, 9, 10545–10562.

[24] De Ceglia, D.; Vincenti, M. A.; De Angelis, C.; Locatelli, A.; Haus, J. W.; Scalora, M. Role of antenna modes and field enhancement in second harmonic generation from dipole nanoantennas. *Opt. Express* **2015**, 23, 1715- 1729.

[25] Celebrano, M.; Wu, X.; Baselli, M.; Großmann, S.; Biagioni, P.; Locatelli, A.; De Angelis, C.; Cerullo, G.; Osellame, R.; Hecht, B.; Duò, L.; Ciccacci, F.; Finazzi, M. Mode matching in multiresonant plasmonic nanoantennas for enhanced second harmonic generation. *Nat. Nanotechnology* **2015**, 10, 412–417.

[26] Dadap, J. I. Optical second-harmonic scattering from cylindrical particles. *Phys. Rev. B* **2008**, 78, 205322.

[27] Shcherbakov, M. R.; Shorokhov, A. S.; Neshev, D. N.; Hopkins, B.; Staude, I.; Melik-Gaykazyan, E. V.; Ezhov, A. A.; Miroshnichenko, A. E.; Brener, I.; Fedyanin, A. A.; Kivshar Y. S. Nonlinear Interference and Tailorable Third-Harmonic Generation from Dielectric Oligomers. *ACS Photonics* **2015**, 2, 578–582.

[28] Shcherbakov, M. R.; Vabishchevich, P. P.; Shorokhov, A. S.; Chong, K. E.; Choi, D.-Y.; Staude, I.; Miroshnichenko, A. E.; Neshev, D. N.; Fedyanin, A. A.; Kivshar, Y. S. Ultrafast All-Optical Switching with Magnetic Resonances in Nonlinear Dielectric Nanostructures. *Nano Lett.* **2015**, 15, 6985–6990.

[29] Yang, Y.; Wang, W.; Boulesbaa, A.; Kravchenko, I. I.; Briggs, D. P.; Puretzky, A.; Geohegan, D.; Valentine, J. Nonlinear Fano-Resonant Dielectric Metasurfaces. *Nano Lett.* **2015**, 15, 7388–7393.

[30] Lee, J.; Tymchenko, M.; Argyropoulos, C.; Chen, P.-Y.; Lu, F.; Demmerle, F.; Boehm, G.; Amann, M.-C.; Alù, A.; Mikhail, A. B. Giant nonlinear response from plasmonic metasurfaces coupled to intersubband transitions. *Nature* **2014**, **511**, 65–69.

[31] Bennemann, K., *Non-linear Optics in Metals*, Clarendon Press, 1998.

[32] Dadap, J. I.; Shan, J.; Eisenthal, K. B.; Heinz, T. F. Second-Harmonic Rayleigh Scattering from a Sphere of Centrosymmetric Material. *Phys. Rev. Lett.* **1999**, 83, 4045–4048.

[33] Makeev, E. V.; Skipetrov, S. E. Second harmonic generation in suspensions of spherical particles. *Opt. Commun.* **2003**, 224, 139–147.

[34] Mäkitalo, J.; Suuriniemi, S.; Kauranen, M. Enforcing symmetries in boundary element formulation of plasmonic and second-harmonic scattering problems. *J. Opt. Soc. Am. A* **2014**, 31, 2821–2832.

[35] Smirnova, D. A.; Khanikaev, A. B.; Smirnov, L. A.; Kivshar, Y. S. Multipolar third-

harmonic generation driven by optically-induced magnetic resonances. ArXiv **2016**, 1601.04109, 1–19.

[36] Gehrsitz, S.; Reinhart, F. K.; Gourgon, C.; Herres, N.; Vonlanthen, A.; Sigg, H. The refractive index of AlxGa1−xAs below the band gap: Accurate determination and empirical modeling. *J. Appl. Phys.* **2000**, 87, 7825–7837.

[37] Terry, F. L. A modified harmonic oscillator approximation scheme for the dielectric constants of Al(x)Ga(1-x)As. *J. Appl. Phys*. **1991**, 70, 409–417.

[38] Shoji, I.; Kondo, T.; Kitamoto, A.; Shirane, M.; Ito, R. Absolute scale of second-order nonlinear-optical coefficients. *J. Opt. Soc. Am. B* **1997**, 14, 2268-2294.

[39] Ohashi. M.; Kondo, T.; Ito, R.; Fukatsu, S.; Shiraki, Y.; Kumata, K.; Kano, S. S. Determination of quadratic nonlinear optical coefficient of $Al_xGa_{1-x}As$ system by the method of reflected second harmonics. *J. Appl. Phys.* **1993**, 74, 596-601

[40] Bautista, G.; Huttunen, M. J.; Mäkitalo, J.; Kontio, J. M.; Simonen, J.; Kauranen, M. Second-harmonic generation imaging of metal nano-objects with cylindrical vector beams. *Nano Lett.* **2012**, 12, 3207–3212.

[41] Bautista, G.; Mäkitalo, J.; Chen, Y.; Dhaka, V.; Grasso, M.; Karvonen, L.; Jiang, H.; Huttunen, M. J.; Huhtio, T.; Lipsanen, H.; Kauranen M. Second-Harmonic Generation Imaging of Semiconductor Nanowires with Focused Vector Beams. *Nano Lett.* **2015**, 15, 1564−1569.

[42] Kerker, M.; Wang, D.-S.; Giles, C. L. Electromagnetic scattering by magnetic spheres. *J. Opt. Soc. Am.* **1983**, 73, 765-767.

TABLE OF CONTENTS GRAPHIC